IEEE Access
Multidisciplinary | Rapid Review | Open Access Journal

SPECIAL SECTION ON POWER ELECTRONICS EMERGING TECHNOLOGIES FOR SUSTAINABLE ENERGY CONSERVATION

Received 18 February 2023, accepted 5 March 2023, date of publication 8 March 2023, date of current version 13 March 2023.

Digital Object Identifier 10.1109/ACCESS.2023.3254306

RESEARCH ARTICLE

Novel Hybrid Modulation Method for Modular Multilevel Converter Based Energy Storage System

DONGDONG CHEN[1,2,3], LONG XIAO[1,3], AND WANQING SONG[1,3]

[1]School of Electronic and Electrical Engineering, Minnan University of Science and Technology, Quanzhou 362700, China
[2]Jiangxi New Energy Technology Institute, Xinyu 338000, China
[3]Key Laboratory of Industrial Automation Control Technology and Application of Fujian Higher Education, Quanzhou 362700, China

Corresponding author: Long Xiao (xdragonl2015@zju.edu.cn)

This work was supported by the Science and Technology Project of Quanzhou City under Grant 2020C011R and Grant 2019CT003.

ABSTRACT This paper focuses on introducing a modular cascaded battery energy storage system and establishing a mathematical model for both the AC and DC sides of the energy storage system. Based on this, a corresponding control strategy is proposed. To achieve a specific trade-off between switching times and output harmonics, a new hybrid modulation strategy (NHPWM) is proposed that combines the characteristics of NLM and CPS-PWM commonly used in traditional modular cascaded topologies. With this hybrid modulation strategy, the modulation of each sub-module can be flexibly configured, allowing the system to coordinate device loss and output harmonic characteristics in real time according to system requirements. Additionally, this paper proposes a calculation method based on the theory of double Fourier series expansion to derive the analytical solution of the NHPWM harmonic distribution, providing a theoretical basis for sub-module modulation mode configuration. Finally, the correctness and effectiveness of the modulation strategy and theoretical calculation were verified by simulation and experiment. The proposed method in this paper has demonstrated clear advantages over traditional HPWM and CPS-PWM in terms of harmonics and efficiency, as shown by the experimental results.

INDEX TERMS Modular multilevel converter (MMC), novel hybrid PWM modulation (NHPWM), nearest level modulation (NLM), carrier phase-shift PWM (CPS-PWM).

I. INTRODUCTION

Energy storage technology plays a crucial role in smoothing renewable energy fluctuations, improving power quality, and enabling large-scale renewable energy integration. It can also support conventional power peak regulation and frequency regulation, and enhance the safety, efficiency, and economy of conventional power generation and transmission. Compared to traditional low-voltage energy storage systems, medium and high voltage large-scale battery energy storage systems are better equipped to perform the essential functions of energy storage technology across various aspects of the power industry. Given the current technical level of battery modules and power devices, modular cascading is a preferable option for medium and high voltage large-scale battery energy storage systems.

Modulation technology is a critical component of the Modular Multilevel Converter (MMC) based energy storage system, as it determines the output characteristics and system efficiency. To maximize the advantages of a modular cascaded energy storage system, a suitable modulation technique must be designed. Pulse Width Modulation (PWM) technology has been extensively studied and various methods have been developed, such as Nearest Level Modulation (NLM) [1], [2], [3], [4], [5], Selected Harmonic Elimination PWM (SHEPWM) [6], [7], Space Vector PWM (SVPWM) [8], [9] and multi-carrier PWM [10], [11]. SHEPWM is suitable for low switching

The associate editor coordinating the review of this manuscript and approving it for publication was Ki-Bum Park.

frequency applications, but calculation of the switching angle is difficult due to the large number of levels. SVPWM has high computational costs and its dynamic response is slower. NLM and multi-carrier PWM are widely used in MMC topology due to simple calculations and comprehensible digital control [12], [13], however, their output voltage error and harmonic content increase as the number of levels decreases. Multi-carrier PWM modulation methods, such as Carrier Level-Shifted PWM (CLS-PWM) and Carrier Phase-Shifted PWM (CPS-PWM), have been proposed to address the imbalance problem of CLS-PWM and to reduce the output harmonic content. Improved frequency-optimized CLS-PWM can balance the sub-modules working status at all levels by selecting the appropriate frequency for the sub-modules carrier at all levels, while CPS-PWM has better output harmonic characteristics.

The traditional modulation techniques have limitations in different application scenarios. To overcome these limitations, hybrid technologies combining different modulation strategies have been proposed. One example is the use of NLM and CPS-PWM in MMC topology [10], which has a unified theoretical form according to study [17]. Another approach is combining NLM and SPWM to improve low-order harmonics and output voltage errors when NLM is applied to MMC topology with a small number of levels, as discussed in [18]. However, this method has disadvantages when the carrier frequency is low, resulting in high output harmonic components [19]. For motor drive applications, a modulation method combining steady-state SHEPWM and transient CPS-PWM has been proposed in Ref. [20]. But in grid-connected applications with relatively severe grid voltage distortion, the current harmonic characteristics of the system output may worsen [21]. It is worth noting that most of the existing literature on harmonic characteristics of hybrid modulation techniques are based on simulation and experimental data, and only a few references provide accurate analytical distribution of corresponding harmonics under the hybrid modulation technology [22].

We have introduced a modular multilevel converter-based battery energy storage system and its mathematical model for the AC/DC sides, which was highly praised by conference attendees [23]. To balance the switching loss and output harmonic characteristics of the system, this paper proposes a novel hybrid PWM (NHPWM) modulation method that combines the commonly used NLM and CPS-PWM modulation methods in conventional cascaded modular multilevel converter topologies. The NHPWM method allows for arbitrary adjustment of the modulation method for each sub-module. Using the double expansion of the Fourier series principle, this paper proposes an analytical solution for the calculation of the NHPWM harmonic distribution to obtain the precise output voltage harmonic distribution of the MMC energy storage system under the proposed NHPWM method. Additionally, a voltage equalization method is presented based on the characteristics of NHPWM, which combines the advantages of the voltage sequencing method and superimposed voltage equalization control components method. The correctness and effectiveness of the proposed method are verified through simulation results and experiments.

The paper is organized as follows. Section II describes the modeling of modular multilevel converter energy storage system, and the mathematical model is established in detail. The principle of NHPWM is presented in Section III, and the harmonic distribution of NHPWM was analyzed theoretically. Experimental results of the proposed NHPWM method are reported in Section IV. Finally, Section V concludes the paper.

II. MODELING OF MODULAR MULTILEVEL CONVERTER ENERGY STORAGE SYSTEM

The topology of the modular multilevel converter-based battery energy storage system is shown in Figure.1. The elements of the circuit represent L_f, r_f, R_d and C_f are passive damping LC output filters on the AC side of the system; L_g and r_g are the line and transformer inductor parameters with the leakage equivalent impedance; r_f and r_g represent the parasitic resistances of L_f and L_g. The grid-connected switch K_2 is closed under normal grid conditions, and the system-side switch K_1 is on/off, according to the on/off-grid working mode. N_c is the number of identical cascaded sub-modules in each phase, and the three-phase system converter is connected by Y-type, which can work in three-wire or four-wire mode to meet the requirements of the application.

The mathematical model of the system in steady state reflects the input and output characteristics of the system. Thus, a rational design of the circuit parameters and control gains can be obtained. Therefore, to ensure the stable and reliable operation of the system, a steady-state mathematical model needs to be established.

The modeling of the modular multilevel converter-based battery energy storage system includes two parts: a model of the system AC side and a model of the system DC side. The mathematical model of the AC side provides the relationship between the modulation wave of the H-bridge part, output voltage, and current of the AC side. For simplicity, the differences in the parameters of the submodule components at all levels were ignored.

The AC-side equivalent circuit of the system is presented in Figure.2, where $u_{ox}(x = a, b, c)$ is the system output voltage after filtering by the system filter, u_x is the one-phase output voltage of the three-phase system converter, and u_{xi} is i-th module output voltage in one phase of the three-phase system, which satisfies Eq.(1):

$$u_{\mathrm{x}} = \sum_{i=1}^{N_{\mathrm{c}}} u_{\mathrm{xi}} \tag{1}$$

The load current i_{Lx} is related to the specific load type, which is regarded as a disturbance of the output current i_{ox}. This study is characterized by the relationship $i_{Lx} = g(u_{ox})$. According to the system AC-side equivalent circuit, the relationship between the voltage and current of the system is

given by the following Eq.(2):

$$\begin{cases} L_{\mathrm{f}}\dfrac{di_{\mathrm{x}}}{dt} = u_{\mathrm{x}} - u_{\mathrm{ox}} - r_{\mathrm{f}} i_{\mathrm{x}} \\ L_{\mathrm{g}}\dfrac{di_{\mathrm{gx}}}{dt} = u_{\mathrm{ox}} - u_{\mathrm{gx}} - r_{\mathrm{g}} i_{\mathrm{gx}} \\ C_{\mathrm{f}}\dfrac{d(u_{\mathrm{ox}} - R_{\mathrm{d}} i_{\mathrm{cx}})}{dt} = i_{\mathrm{cx}} \\ i_{\mathrm{x}} = i_{\mathrm{ox}} + i_{\mathrm{cx}} = i_{\mathrm{Lx}} + i_{\mathrm{gx}} + i_{\mathrm{cx}} \end{cases} \tag{2}$$

In this study, we mainly discuss the control strategy of a modular multilevel converter-based battery energy storage system based on a voltage source, with the aim of controlling the output voltage u_{ox} of the system. To calculate the filtered terminal voltage u_{ox}, we apply the Laplace transform to Eq.(2) and obtain

$$u_{ox}(s) = \frac{g_{\mathrm{Lf}}(s)u_x(s) + g_{\mathrm{Lg}}(s)u_{gx}(s) - i_{\mathrm{Lx}}(s)}{g_{\mathrm{Lf}}(s) + g_{\mathrm{cf}}(s) + g_{\mathrm{Lg}}(s)} \tag{3}$$

where $g_{Lf}(s)$, $g_{cf}(s)$, and $g_{Lg}(s)$ are the admittances of the three branches of r_f and L_f, R_d and C_f, r_g and L_g, respectively. The impedances of the three branches are denoted as $Z_{Lf}(s)$, $Z_{cf}(s)$, and $Z_{Lg}(s)$ as follows:

$$\begin{cases} Z_{\mathrm{Lf}}(s) = \dfrac{1}{g_{\mathrm{Lf}}(s)} = sL_{\mathrm{f}} + r_{\mathrm{f}} \\ Z_{\mathrm{Cf}}(s) = \dfrac{1}{g_{\mathrm{Cf}}(s)} = \dfrac{1}{sC_{\mathrm{f}}} + R_{\mathrm{d}} \\ Z_{\mathrm{Lg}}(s) = \dfrac{1}{g_{\mathrm{Lg}}(s)} = sL_{\mathrm{g}} + r_{\mathrm{g}} \end{cases} \tag{4}$$

In the battery energy storage system, v_{dc_xi} and SOC_{xi} are the terminal voltage and the State of Charge (SOC) of the x phase (x for A, B, C phase) i-th battery modul. For simplicity, the relationship between v_{dc_xi} and SOC_{xi} can be regarded as approximately linear, which is presented as follows:

$$v_{\mathrm{dc\_xi}} = V_{\mathrm{dc0}} + k_{\mathrm{vs}} SOC_{\mathrm{xi}} \tag{5}$$

In the Eq.(5), V_{dc0} is the terminal voltage when the SOC is equal to 0 in the linear segment of the OCV-SOC curve and k_{vs} is the slope of the linear segment. Thus, the average value of the DC side voltage of the three phases is V_{dc_avg}, the module average voltage value in the phase of each phase is V_{dc_avgx}, the three-phase average state of charge SOC_{avg}, and the module average state of charge in the phase SOC_{avg_x} of each phase are related to Eq.(6):

$$\begin{cases} SOC_{\mathrm{avgx}} = \dfrac{1}{N_{\mathrm{c}}}\displaystyle\sum_{i=1}^{N_{\mathrm{c}}} SOC_{\mathrm{xi}} \\ SOC_{\mathrm{avg}} = \dfrac{1}{3}\displaystyle\sum_{x=a}^{c} SOC_{\mathrm{avgx}} \end{cases}$$
$$\begin{cases} V_{\mathrm{dc\_avgx}} = \dfrac{1}{N_{\mathrm{c}}}\displaystyle\sum_{i=1}^{N_{\mathrm{c}}} v_{\mathrm{dc\_xi}} = V_{\mathrm{dc0}} + k_{\mathrm{vs}} SOC_{\mathrm{avgx}} \\ V_{\mathrm{dc\_avg}} = \dfrac{1}{3}\displaystyle\sum_{x=a}^{c} v_{\mathrm{dc\_avgx}} = V_{\mathrm{dc0}} + k_{\mathrm{vs}} SOC_{\mathrm{avg}} \end{cases} \tag{6}$$

Therefore, in the linear region of the OCV-SOC curve, the equalization control of the sub-module SOC is approximately equivalent to the equalization control of the terminal voltage. During operation:

$$\begin{cases} \Delta v_{\mathrm{dc\_xi}} = v_{\mathrm{dc\_xi}} - v_{\mathrm{dc\_avgx}} \\ \displaystyle\sum_{i=1}^{N_{\mathrm{c}}} u_{\mathrm{xi}} = u_{\mathrm{x}} \rightarrow \sum_{i=1}^{N_{\mathrm{c}}} v_{\mathrm{s\_xi}} = v_{\mathrm{sx}} \end{cases} \tag{7}$$

Δv_{dc_xi} is the difference between i-th sub-module voltage and the average voltage V_{dc_avgx}; v_{s_xi} and v_{s_x} are the i-th sub-module modulation voltages and phase-x (x for phases A, B, and C) overall modulation voltages, respectively. When the system is operating, the sum of the sub-module modulation voltages must be equal to the overall modulation voltage of the corresponding phase. The energy storage system SOC balance of each module includes phase-to-phase balance and module-to-module balance in the same phase. According to Eq.(7), phase-to-phase balance can be achieved by adjusting the overall modulation voltage v_{sx} of each phase. Module-to-module balance was achieved by adjusting the sub-module modulation voltage v_{sx} of each module in the phase. The implementation process is described in detail in the following section.

III. PROPOSED NOVEL HYBRID MODULATION STRATEGY FOR MMC ENERGY STORAGE SYSTEM

A. PRINCIPLE OF NHPWM

For the modular multilevel converter, it is assumed that the DC-link voltage of each submodule is V_{dc}, the grid voltage peak value is U_{sm}, and the number of cascaded submodules must be $N_{\mathrm{c}} \geq \lceil U_{\mathrm{sm}} \rceil / V_{\mathrm{dc}}$. When using nearest-level modulation (NLM), the number of switching times is small and the implementation is simple. However, when this modulation strategy is applied to situations with a small number of MMC modules, the output voltage error of the system is relatively large. For this reason, some scholars have conducted research on hybrid modulation strategies (HPWM). Based on NLM, this modulation strategy divides N_c cascaded modules into $N_c - 1$ NLM modulation modules and one SPWM modulation module. The $N_c - 1$ modules operate in NLM mode, and the remaining 1 module working in unipolar frequency-doubling SPWM modulation mode to achieve the goal of output voltage zero error. The output voltage for this modulation strategy is shown in Figure.3. Although this method can solve the problem of output voltage error, the equivalent switching frequency of the system output voltage is limited to 2 times the switching frequency. Therefore, this method cannot take full advantage of multilevel topology; when applied to high-power low-switching frequency applications with a small number of modules, a large output filter must be designed for the system.

Therefore, a novel hybrid PWM modulation strategy (NHPWM) is proposed in this paper. The key part of NHPWM is that the number of PWM modulation modules is no longer limited to one, but $N_p \in [0, N_c]$ modules can

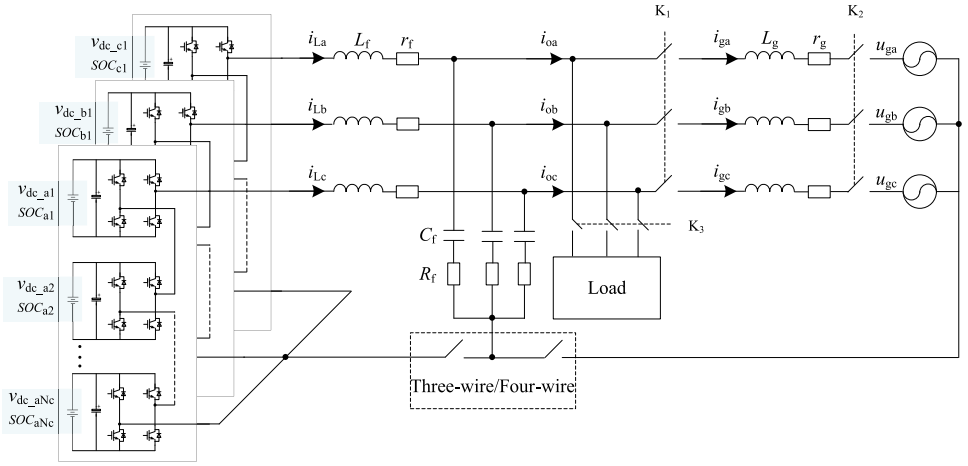

FIGURE 1. Topology of the modular multilevel converter based battery energy storage system.

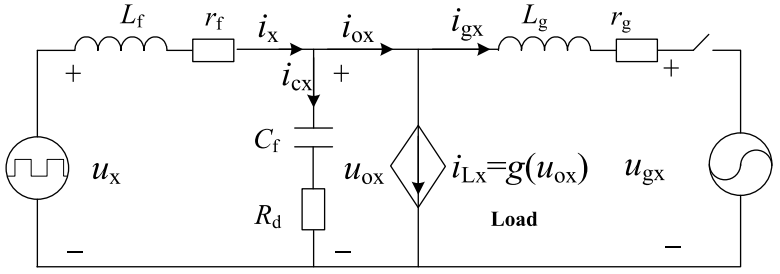

FIGURE 2. Grid-connected equivalent circuit on the AC side of the system.

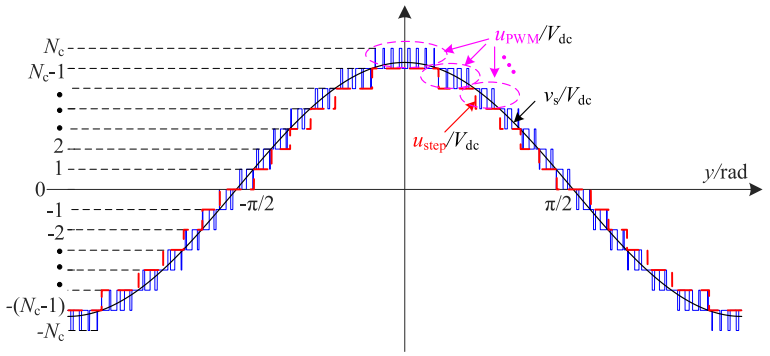

FIGURE 3. The normalized waveform of the direct output voltage of the converter under HPWM.

be flexibly modulated by the CPS-PWM method, and the remaining $(N_c - N_P)$ submodules adopt NLM modulation. When $N_p = 0$, NHPWM degenerates into NLM modulation; when $N_p = 1$, NHPWM is equivalent to HPWM; and when $N_p = N_c$, NHPWM becomes pure CPS-PWM modulation. The NHPWM output voltage is point out in Figure.4 when $N \in [1, N_c]$.

To simplify the analysis, this study assumes that the DC-link voltage of each submodule is equal to V_{dc}. Where M is the modulation ratio of the system, and y is the phase of the modulation voltage of each module. Thus, the overall modulation voltage v_s can be obtained using Eq.(8).

$$v_{\mathrm{s}} = MN_{\mathrm{c}}V_{\mathrm{dc}}\cos y = MN_{\mathrm{c}}V_{\mathrm{dc}}\cos\omega_{\mathrm{N}}t \tag{8}$$

When the NHPWM strategy is used for modulation, the principles of the two strategies included in NHPWM are different. Therefore, the submodule must be separated into two parts for the analysis. In this study, the output voltages after NLM modulation and CPS-SPWM modulation are defined as the step wave u_{step} and PWM wave u_{PWM} respectively, as shown in Figure.3. Regardless of the dead and switching times, the ideal MMC one-phase output voltage u_x satisfies Eq.(9) below.

$$u_{\mathrm{x}} = u_{\mathrm{step}} + u_{\mathrm{PWM}} \tag{9}$$

Second, the sub-modules that work in NLM mode are switched on and off according to the requirements of voltage

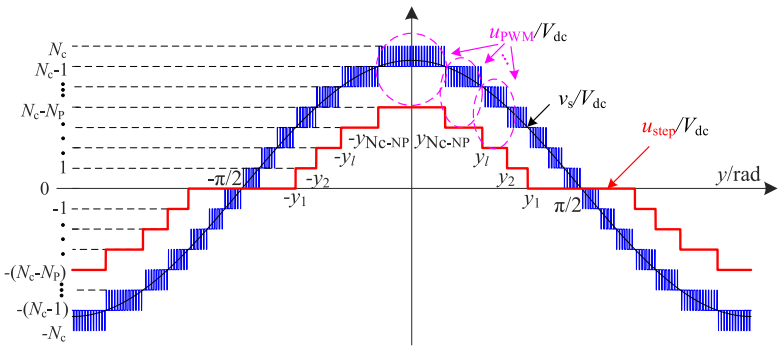

FIGURE 4. The normalized waveform of the direct output voltage of the converter under NHPWM.

equalization, and the remaining sub-modules configured as CPS-PWM are carried out according to the principle of the traditional CPS-PWM strategy of multilevel topology with N_p sub-modules cascaded pulse width modulation. Therefore, the initial voltage y_l at the output l level of u_{step} generated by the (N_c-N_P) sub-modules, which operate in the NLM mode, can be calculated as shown in Figure.4. u_{step} is the l-level output of a specific initial position y_l, y_l can be calculated using Eq.(10) below.

$$y_l = \begin{cases} \pi/2, & l = 0 \\ \dfrac{\arccos(l + N_P - 1)}{N_c M}, & N_c M > l + N_P - 1 \;\&\; l \neq 0 \\ 0, & N_c M \leq N_P \;\&\; l \neq 0 \end{cases} \tag{10}$$

Then, the sub-modules operate in the CPS-PWM mode, whose module number is $N_p \in [1, N_c]$. When the voltage equalization control component is not considered, the modulation voltage v_P of the N_p submodules is consistent; it can be obtained using the formula below. Where $\lceil\rceil$ is an integer operator and sgn is a symbolic function.

$$v_P = \begin{cases} \dfrac{N_c M \cos y - \mathrm{sgn}(\cos y)\,[\lceil |N_c M \cos y| \rceil - N_P]}{N_P} V_{dc}, & \lceil |N_c M \cos y| \rceil \geq N_P \\ \dfrac{N_c M \cos y}{N_P} V_{dc}, & \lceil |N_c M \cos y| \rceil < N_P \end{cases} \tag{11}$$

Based on the theory of H-bridge unipolar frequency doubling modulation, assuming that the modulation voltage of the H-bridge left bridge arm is v_p, the modulation voltage of the H-bridge right bridge arm is -v_p. The normalized voltages of the two modulation waves can be acquired as Figure.5. It can be observed from Figure.5, that v_P is an irregular curve, but it is still a periodically repeating wave with a fundamental period.

Figure.6 shows the modulation process within a carrier period $T_c = 1/f_c$ in the CPS-PWM mode, where x represents the phase of the carrier u_i (i = 1,2,…, N_P). u_{L1} and u_{R1} are the output voltages of the left and right bridge arms of the first module working in the CPS-PWM mode. Therefore, $u_{PWM1} = u_{L1}$-u_{R1} is the output voltage of the module-PWM modulation.

The output voltage $u_{PWM\_i}(i = 2, 3, \ldots, N_P)$ of other sub-modules with the CPS-PWM mode, whose number is($N_P - 1$), can be calculated by shifting a certain angle of u_{PWM1} in theory. Then, the output voltage of the N_P sub-modules with the CPS-PWM mode is calculated using Eq.(12) below.

$$u_{PWM} = \sum_{i=1}^{N_P} u_{PWM\_i} \tag{12}$$

B. OUTPUT HARMONIC CHARACTERISTICS OF NHPWM

To accurately evaluate the output harmonic characteristics of the proposed NHPWM modulation strategy, the mathematical derivation method for the output harmonic characteristics of NHPWM is given below, and an analytical solution of the harmonic distribution of the converter output voltage is obtained. According to the principle of superposition, the solution to the harmonic distribution of the converter output voltage u_x can be decomposed into separate solutions u_{step} and u_{PWM} of the harmonic distributions. In the following, we assume that n is an integer number, and m is a positive integer number $m \in \mathbb{Z}^+$.

u_{step} can be expanded into the Fourier series shown in Eq.(13)

$$u_{step} = \sum_{n=-\infty}^{\infty} C_n e^{jn\omega_N t} \tag{13}$$

The coefficient C_n reads as follows:

$$\begin{aligned} C_n &= \frac{1}{2\pi} \int_{-\pi}^{\pi} u_{step} e^{-jn\omega_N t} d\omega_N t \\ &= \frac{2u_d}{n\pi} \sum_{l=1}^{N-N_P} \begin{cases} \sin n y_l & n = odd \\ 0 & n = even \end{cases} \end{aligned} \tag{14}$$

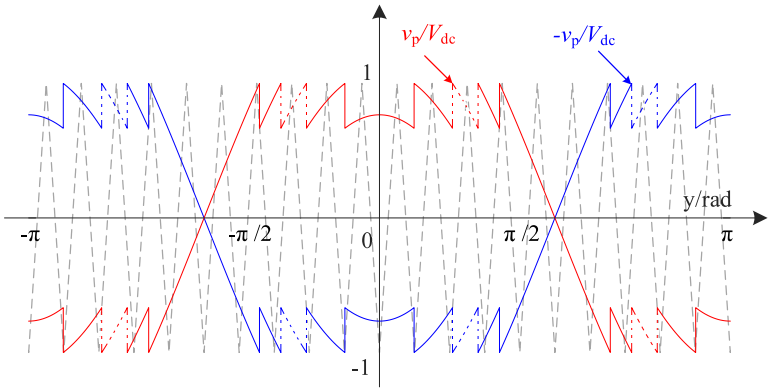

FIGURE 5. Normalized modulation waveform of H-bridge sub-module in CPS-PWM mode.

It is clear from Eq.(14), C_n is symmetric about n: $C_n = C_{-n}$. So there are:

$$C_{-n}e^{j(-n)\omega_1 t} + C_n e^{jn\omega_1 t} = 2C_n \cos n\omega_N t = 2C_n \cos ny \tag{15}$$

Substituting (14) and (15) into (13), we obtain

$$u_{\text{step}} = \sum_{n=1,3,5}^{\infty} \frac{4V_{\text{dc}}}{n\pi} \sum_{l=1}^{N_c-N_P} \sin ny_l \cos ny \tag{16}$$

From Eq.(16), under NLM modulation, the output ladder wave u_{step} must contain low-frequency odd-order harmonics. Using only NLM modulation causes the output voltage to contain certain low-order harmonics. u_{PWM} is the sum of the output voltages of the modules in N_P CPS PWM modes. To solve the harmonic distribution of u_{PWM}, the solution of $u_{\text{PWM\_i}}$ should first be analyzed. The harmonic distribution of $u_{\text{PWM\_i}}$ is affected by the four switching angles $\theta_{iq}(q = 1, 2, 3, 4)$. It can also be observed that the switch angle of module i differs from that of module 1 by only a specific phase-shift angle:

$$\theta_{\text{iq}} = \theta_{1\text{q}} + (i-1)\pi/N_{\text{P}}, \quad i = 1, 2, \ldots, N_{\text{P}} \;\; q = 1, 2, 3, 4 \tag{17}$$

Therefore, the four switching angles corresponding to the module's output voltage in the i-th CPS-PWM mode can be obtained according to the modulation process shown in Figure.4 and the relationship shown in Eq.(17), as shown in Table.1.

It is clear from Figure.4 that carrier u_{ci} and modulation voltage v_p are functions of phases x and y, respectively. Therefore, the output voltage u_{PWM_i} after the CPS-PWM modulation of the i-th submodule becomes a binary function $u_{PWM\_i}(x, y)$. The expression below provides the value of $u_{PWM\_i}(x, y)$ for different intervals.

$$u_{\text{PWM\_i}}(x, y) = \sum_{l=1}^{N_c-N_P+1} \begin{cases} V_{\text{dc}} & x \in [\theta_{i1}, \theta_{i3}] \cup [\theta_{i4}, \theta_{i2}] \;\&\; \\ & y \in (-y_{l-1}, -y_l) \cup (y_l, y_{l-1}) \\ -V_{\text{dc}} & x \in [\theta_{i3}, \theta_{i1}] \cup [\theta_{i2}, \theta_{i4}] \;\&\; \\ & y \in (\pi - y_{l-1}, \pi - y_l) \\ & \quad \cup (-(\pi - y_l), -(\pi - y_{l-1})) \\ 0 & others \end{cases} \tag{18}$$

Clearly, the function $u_{PWM\_i}(x, y)$ must satisfy the Dirichlet boundary condition. Then, by applying a double Fourier series to Eq.(18), we obtain the following expression:

$$\begin{aligned} &u_{\text{PWM\_i}} \\ &= A_{00\_\text{i}}/2 + \sum_{n=1}^{\infty} [A_{0\text{n\_i}} \cos ny + B_{\text{on\_i}} \sin ny] \\ &\quad + \sum_{m=1}^{\infty} [A_{\text{m0\_i}} \cos mx + B_{\text{m0\_i}} \sin mx] \\ &\quad + \sum_{m=1}^{\infty} \sum_{n=\pm 1}^{\pm\infty} [A_{\text{mn\_i}} \cos(mx + ny) + B_{\text{mn\_i}} \sin(mx + ny)] \\ &= \sum_{n=1}^{\infty} A_{0\text{n\_i}} \cos ny + \sum_{m=1}^{\infty} A_{\text{m0\_i}} \cos mx \\ &\quad + \sum_{m=1}^{\infty} \sum_{n=\pm 1}^{\pm\infty} A_{\text{mn\_i}} \cos(mx + ny) \end{aligned} \tag{19}$$

Here the coefficients A_{mn_i} and B_{mn_i} satisfy the condition for complex coefficient C_{mn_i}:

$$\begin{aligned} C_{\text{mn\_i}} &= A_{\text{mn\_i}} + \text{j}B_{\text{mn\_i}} = A_{\text{mn\_i}} \\ &= 1/2\pi^2 \int_{-\pi}^{\pi} \int_{\pi}^{\pi} u_{\text{PWM\_i}}(x, y) e^{\text{j}(mx+ny)} dxdy \end{aligned} \tag{20}$$

Recalling to the symmetry of $u_{\text{ci}}(x)$ and $v_{\text{p}}(y)$, the imaginary part of C_{mn_i} must be equal to 0, i.e., $C_{mn\_i} = A_{mn\_i}$. And because u_{PWM_i} is positive and negative symmetrical, there is no DC component, so $A_{00\_i} = 0$. Substituting Eq.(18) into

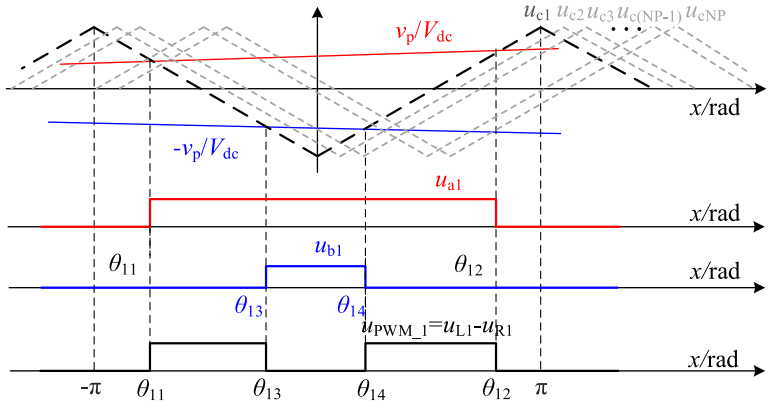

FIGURE 6. CPS-PWM modulation process.

TABLE 1. The switching angle of the module in the *i*-th CPS-PWM mode.

θ_{iq}	Modulation voltage phase $y\in(-y_{l-1},-y_l)\cup(y_l,y_{l-1})$	θ_{iq}	Modulation voltage phase $y\in(\pi-y_{l-1},\pi-y_l)\cup(-(\pi-y_l),-(\pi-y_{l-1}))$
θ_{i1}	$-\pi(N_cM\cos y-l+1+N_P)/2N_P+\pi(i-1)/N_P$	θ_{i1}	$-\pi(N_cM\cos y+l-1+N_P)/2N_P+\pi(i-1)/N_P$
θ_{i2}	$\pi(N_cM\cos y-l+1+N_P)/2N_P+\pi(i-1)/N_P$	θ_{i2}	$\pi(N_cM\cos y+l-1+N_P)/2N_P+\pi(i-1)/N_P$
θ_{i3}	$\pi(N_cM\cos y-l+1-N_P)/2N_P+\pi(i-1)/N_P$	θ_{i3}	$\pi(N_cM\cos y+l-1-N_P)/2N_P+\pi(i-1)/N_P$
θ_{i4}	$-\pi(N_cM\cos y-l+1-N_P)/2N_P+\pi(i-1)/N_P$	θ_{i4}	$-\pi(N_cM\cos y+l-1-N_P)/2N_P+\pi(i-1)/N_P$

Eq.(20) yields Eq.(21).

$$
\begin{aligned}
&A_{\mathrm{mn\_i}}\\
&=\sum_{l=1}^{N_c-N_P+1}\frac{1}{2\pi^2}\int_{-\pi}^{\pi}\int_{-\pi}^{\pi}u_{l\_i}(x,y)e^{\mathrm{j}(mx+ny)}dxdy\\
&=\sum_{l=1}^{N-P+1}\frac{V_{dc}}{2\pi^2}\left\{\begin{array}{l}
\displaystyle\int_{-y_{l-1}}^{-y_l}\left[\int_{\theta_{i1}}^{\theta_{i3}}e^{\mathrm{j}(mx+ny)}dx+\int_{\theta_{i4}}^{\theta_{i2}}e^{\mathrm{j}(mx+ny)}dx\right]dy\\
\displaystyle+\int_{y_l}^{y_{l-1}}\left[\int_{\theta_{i1}}^{\theta_{i3}}e^{\mathrm{j}(mx+ny)}dx+\int_{\theta_{i4}}^{\theta_{i2}}e^{\mathrm{j}(mx+ny)}dx\right]dy\\
\displaystyle+\int_{-(\pi-y_{l-1})}^{-(\pi-y_l)}\left[\int_{\theta_{i3}}^{\theta_{i1}}-e^{\mathrm{j}(mx+ny)}dx+\int_{\theta_{i2}}^{\theta_{i4}}-e^{\mathrm{j}(mx+ny)}dx\right]dy\\
\displaystyle+\int_{\pi-y_l}^{\pi-y_{l-1}}\left[\int_{\theta_{i3}}^{\theta_{i1}}-e^{\mathrm{j}(mx+ny)}dx+\int_{\theta_{i2}}^{\theta_{i4}}-e^{\mathrm{j}(mx+ny)}dx\right]dy
\end{array}\right.
\end{aligned}
\tag{21}
$$

The Eq.(21), the calculation result is discussed according to whether m is 0, namely A_{0n_i} and A_{mn_i} $(m\neq 0)$. To facilitate the calculation, we define two functions, $T_i(y)$ and $H_i(y)$, as shown in Eq.(22) and Eq.(23).

$$
\begin{aligned}
T_{\mathrm{i}}(y)&=e^{\mathrm{j}m\theta_{i3}}-e^{\mathrm{j}m\theta_{i1}}+e^{\mathrm{j}m\theta_{i2}}-e^{\mathrm{j}m\theta_{i4}}\\
&=\left\{\begin{array}{ll}
4\mathrm{j}e^{\mathrm{j}m(i-1)\pi/N_P}\cos(m\pi/2)\sin[m\pi(N_cM\cos y & \\
\quad -l+1)/2N_P], & m=even\ \&\ m\neq 0\\
0, & m=odd
\end{array}\right.
\end{aligned}
\tag{22}
$$

$$
\begin{aligned}
H_i(y)&=\theta_{i3}-\theta_{i1}+\theta_{i2}-\theta_{i4}\\
&=-2\pi(N_cM\cos y+l-1)/N_P
\end{aligned}
\tag{23}
$$

By substituting Eq.(22) and Eq.(23) into Eq.(21), the coefficients $A_{mn\_i}(m\neq 0)$ and A_{0n_i} take the following form:

$$
\begin{aligned}
A_{\mathrm{mn\_i}}=\frac{V_{dc}}{\mathrm{j}\pi^2 m}\sum_{l=1}^{N-N_P+1}\int_{y_l}^{y_{l-1}}&[T_{\mathrm{i}}(y)\cos ny\\
&+T_{\mathrm{i}}(\pi-y)\cos(n\pi-ny)]dy,\ m\neq 0
\end{aligned}
\tag{24}
$$

$$
\begin{aligned}
A_{0\mathrm{n\_i}}=\frac{V_{dc}}{\pi^2}\sum_{l=1}^{N_c-N_P+1}\int_{y_l}^{y_{l-1}}&[H_1(y)\cos ny\\
&+H_1(\pi-y)\cos(n\pi-ny)]dy
\end{aligned}
\tag{25}
$$

Note that the value of A_{mn_i} is related to index i, which makes the integral calculation of Eq.(24) difficult. Let $A_{\mathrm{mn}} = \sum_{i=1}^{N_\mathrm{P}} A_{\mathrm{mn\_i}}$ be the result of A_{mn} being calculated directly. By exchanging the summation symbols, (26) can be derived as

$$\begin{aligned} u_{\mathrm{PWM}} &= \sum_{i=1}^{N_\mathrm{P}} u_{\mathrm{PWM\_i}} \\ &= \sum_{i=1}^{N_\mathrm{P}} \sum_{n=1}^{\infty} A_{\mathrm{0n\_i}} \cos ny + \sum_{i=1}^{N_\mathrm{P}} \sum_{m=1}^{\infty} A_{\mathrm{m0\_i}} \cos mx \\ &\quad + \sum_{i=1}^{N_\mathrm{P}} \sum_{m=1}^{\infty} \sum_{n=\pm 1}^{\pm\infty} A_{\mathrm{mn\_i}} \cos(mx+ny) \\ &= \sum_{n=0}^{\infty} A_{\mathrm{0n}} \cos ny + \sum_{m=1}^{\infty} A_{\mathrm{m0}} \cos mx \\ &\quad + \sum_{m=1}^{\infty} \sum_{n=\pm 1}^{\pm\infty} A_{\mathrm{mn}} \cos(mx+ny) \end{aligned} \tag{26}$$

By combining Eq.(22) and Eq.(24), we note that for $m \neq 0$, the coefficient A_{mn_i} is not zero only if m is an even number. Therefore, the following only needs to discuss the case where m is an even number: Eq.(27) is derived when m is an even number.

$$\begin{aligned} A_{mn} &= \sum_{i=1}^{N_\mathrm{P}} A_{\mathrm{mn\_i}} = \sum_{i=1}^{N_\mathrm{P}} \frac{V_{\mathrm{dc}}}{\mathrm{j}\pi^2 m} \sum_{l=1}^{N_\mathrm{c}-N_\mathrm{P}+1} \int_{y_l}^{y_{l-1}} \\ &\quad \times [T_{\mathrm{i}}(\pi - y)\cos(n\pi - ny) + T_{\mathrm{i}}(y)\cos ny]dy \\ &= \begin{cases} \dfrac{8V_{\mathrm{dc}}}{\pi^2 m} \cos\dfrac{m\pi}{2} \left(\sum\limits_{i=1}^{N_\mathrm{P}} e^{j\frac{m(i-1)\pi}{N_\mathrm{P}}} \right) \sum\limits_{l=1}^{N_\mathrm{c}-N_\mathrm{P}+1} \int_{y_l}^{y_{l-1}} \\ \quad \times \cos\dfrac{m(l-1)\pi}{2N_\mathrm{P}} \cos\dfrac{m\pi(N_\mathrm{c}M\cos y)}{2N_\mathrm{P}} \cos nydy, \\ \qquad\qquad n = \pm 1, \pm 3, \ldots \\ -\dfrac{8V_{\mathrm{dc}}}{\pi^2 m} \cos\dfrac{m\pi}{2} \left(\sum\limits_{i=1}^{N_\mathrm{P}} e^{j\frac{m(i-1)\pi}{N_\mathrm{P}}} \right) \sum\limits_{l=1}^{N_\mathrm{c}-P+1} \int_{y_l}^{y_{l-1}} \\ \quad \times \sin\dfrac{m(l-1)\pi}{2N_\mathrm{P}} \sin\dfrac{m\pi(N_\mathrm{c}M\cos y)}{2N_\mathrm{P}} \cos nydy, \\ \qquad\qquad n = \pm 2, \pm 4, \ldots \end{cases} \end{aligned} \tag{27}$$

The term $\sum_{i=1}^{N_\mathrm{P}} e^{\mathrm{j}\frac{m(i-1)\pi}{N_\mathrm{P}}}$ in (27) represents the summation of geometric sequences, that is, $\sum_{i=1}^{N_\mathrm{P}} e^{\mathrm{j}\frac{m(i-1)\pi}{N_\mathrm{P}}} = \frac{1-e^{jm\pi}}{1-e^{\frac{jm\pi}{N_\mathrm{P}}}}$. In particular, for $m = 2kN_\mathrm{P}$ (k is a natural number), the denominator is equal to 0. Thus, the idea of seeking the limit is adopted, and the value at $m = 2kN_\mathrm{P}$ (k is a positive integer) is solved using Eq.(28).

$$\begin{aligned} &\sum_{i=1}^{N_\mathrm{P}} e^{\mathrm{j}\frac{m(i-1)\pi}{N_\mathrm{P}}} \\ &= \begin{cases} \lim\limits_{m\to 2kN_\mathrm{P}} \dfrac{1-e^{jm\pi}}{1-e^{\frac{jm\pi}{N_\mathrm{P}}}}, & m = 2kN_\mathrm{P} \\ 0, & m = 2k, m \neq 2kN_\mathrm{P} \end{cases} \\ &= \begin{cases} N_\mathrm{P} e^{jm(N_\mathrm{P}-1)\pi/N_\mathrm{P}} = N_\mathrm{P}, & m = 2kN_\mathrm{P} \\ 0, & m = 2k, m \neq 2kN_\mathrm{P} \end{cases} \end{aligned} \tag{28}$$

If and only when $m = 2kN_P$ and n is an odd number, the value of $A_{mn}(m \neq 0)$ is not 0. That is, $A_{mn}(m \neq 0)$ can be further simplified to Eq.(29).

$$A_{mn} = \begin{cases} \dfrac{8N_\mathrm{P}V_{\mathrm{dc}}}{\pi^2 m} \cos\dfrac{m\pi}{2} \sum\limits_{l=1}^{N_\mathrm{c}-N_\mathrm{P}+1} \int_{y_l}^{y_{l-1}} \cos\dfrac{m(l-1)\pi}{2N_\mathrm{P}} \\ \quad \times \cos\dfrac{m\pi(N_\mathrm{c}M\cos y)}{2N_\mathrm{P}} \cos nydy, \\ \quad m \neq 0 \ \&\ m = 2kN_\mathrm{P} \ \&\ n = \text{odd} \\ 0, \quad \text{others} \end{cases} \tag{29}$$

In order to solve Eq.(29), we adopted the Jacobi-Anger series expansion. In Eq.(30), $J_k(\lambda)$ represents the k-th Bessel function.

$$\begin{aligned} e^{\pm j\lambda\cos\theta} &= J_0(\lambda) + 2\sum_{k=1}^{\infty} j^{\pm k} J_k(\lambda)\cos k\theta \Rightarrow \sin(\lambda\cos\theta) \\ &= 2\sum_{k=1,3,5\ldots}^{\infty} \sin(k\pi/2) J_k(\lambda)\cos k\theta \end{aligned} \tag{30}$$

According to Eq.(30), $A_{\mathrm{mn}}(m \neq 0, m = 2kN_\mathrm{P}, n$ is an odd number) can be further derived as follows: (31) shown at the bottom of the next page.

The solving process of A_{0n} is similar to that of A_{mn} and will not be described in detail. The expansion result of A_{0n} is shown in Eq.(32).

$$\begin{aligned} A_{0n} &= \sum_{i=1}^{N_\mathrm{P}} A_{\mathrm{0n\_i}} \\ &= \begin{cases} -\sum\limits_{n=1,3,5}^{\infty} \dfrac{4V_{\mathrm{dc}}}{n\pi} \sum\limits_{l=1}^{N_\mathrm{c}-N_\mathrm{P}} \sin ny_l, & n = 3, 5, 7, \ldots \\ N_\mathrm{c}MV_{\mathrm{dc}} - \dfrac{4V_{\mathrm{dc}}}{\pi} \sum\limits_{l=1}^{N_\mathrm{c}-N_\mathrm{P}+1} \sin y_l, & n = 1 \end{cases} \end{aligned} \tag{32}$$

Substituting A_{mn} solution results (31) and (32) into Eq. (26), the u_{PWM} double Fourier series expansion can be solved. The expansion results of u_{step} and u_{PWM} were superimposed. The Fourier series expansion of the converter output phase voltage u_x under NHPWM modulation can be obtained as shown in Eq.(33).

$$\begin{aligned} u_{\mathrm{x}} &= u_{\mathrm{step}} + u_{\mathrm{PWM}} \\ &= u_{\mathrm{step}} + \sum_{i=1}^{N_\mathrm{P}} u_{\mathrm{PWM\_i}} \\ &= N_\mathrm{c}MV_{\mathrm{dc}}\cos y \end{aligned}$$

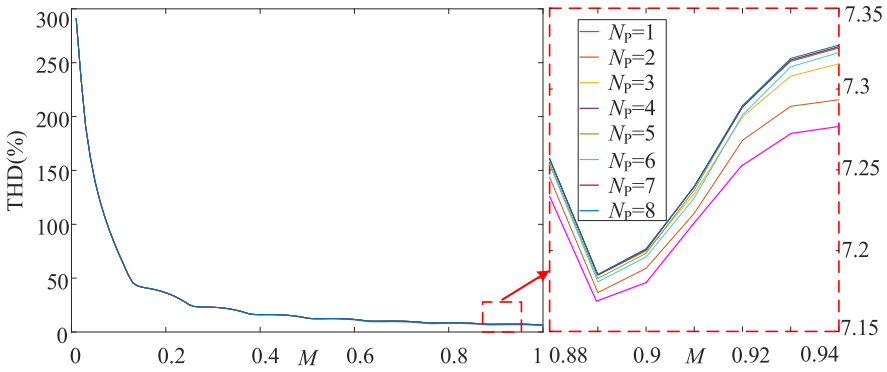

FIGURE 7. CPS-PWM modulation process Total harmonic distortion–modulation ratio *M* curve for different N_p.

$$+\sum_{m=2N_{\mathrm{P}},4N_{\mathrm{P}},6N_{\mathrm{P}}}^{\infty}\ \sum_{n=\pm1,\pm3,\pm5}^{\infty}[A_{\mathrm{mn}}\cos(mx+ny)] \quad (33)$$

The following conclusions can be drawn from Eq.(33):

(1) The direct output voltage u_x of the converter did not contain even harmonics.

(2) For $N_p \in [1, N_c]$, u_x does not contain low-order harmonics, indicating that NHPWM can eliminate the low-order harmonics caused by step wave u_{step} under NLM modulation; that is, NHPWM should ensure that at least one module works in CPS-PWM mode.

(3) The harmonics of u_x are concentrated in the odd frequency band of $2kN_Pf_c$, that is, the equivalent switching frequency of the output voltage u_x under NHPWM is increased to $2kN_P$ times the carrier frequency f_c, which is conducive to the on-demand design of the output filter.

According to the definition of the total harmonic distortion (THD), the THD of the output voltage u_x can be calculated using Eq.(34):

$$\mathrm{THD}=\frac{\sqrt{\sum_{m=2N_{\mathrm{P}},4N_{\mathrm{P}},6N_{\mathrm{P}}}^{\infty}\ \sum_{n=\pm1,\pm3,\pm5}^{\infty}A_{\mathrm{mn}}^2}}{N_{\mathrm{c}}MV_{\mathrm{dc}}}\times100\% \quad (34)$$

The number of cascaded modules $N_c = 8$ and the carrier frequency f_c was 40 times the fundamental frequency f_N. According to Eq.(34), Figure.7 shows the relationship curve between the THD of u_x and the modulation ratio M under different N_P. As shown in the figure, as the modulation ratio M increased, the THD gradually decreased. This is because an increase in M causes the number of output levels to gradually increase, and the calculation result is consistent with the actual situation. In addition, it can be seen that when N_P changes from 1 to N_c, the curves are essentially the same. The calculation errors mainly caused slight differences. That is, the configuration of the modulation mode does not affect the total harmonic content of u_x. This will only affect the distribution characteristics of its harmonics, which is conducive to the targeted adjustment of the modulation mode distribution under NHPWM according to the design constraints, such as the heat dissipation of the system and the volume of the filter.

IV. EXPERIMENTAL VALIDATION

To verify the effectiveness and engineering practicability of the proposed NHPWM modulation and harmonic calculation method. A modular multilevel converter-based battery energy storage system prototype, whose parameters are listed in Table.2, was built in a laboratory. The prototype was mainly composed of battery modules in the DC-link and modular cascaded multilevel converters. On this basis, the experimental platform required in this study also includes a programmable AC power supply, local passive load, and corresponding measuring instruments. A photograph of the prototype is presented in Figure.8.

In this study, the experiment verifies the NHPWM modulation strategy of the modular cascaded energy storage system and the output voltage control and voltage equalization control based on this modulation strategy. To eliminate the influence of harmonics in the grid voltage on the analysis of the harmonic distribution of the direct output voltage u_x of the MMC converter, the experiment in this article is an island load mode, the local load is a pure resistance-capacitance

$$A_{mn}=\frac{8N_{\mathrm{P}}V_{\mathrm{dc}}}{\pi^2 m}\cos\frac{m\pi}{2}\sum_{l=1}^{N_{\mathrm{c}}-N_{\mathrm{P}}+1}\left[\begin{array}{l}\cos\dfrac{m(l-1)\pi}{2N_{\mathrm{P}}}\displaystyle\sum_{k=1,3,5}^{\infty}\sin\frac{k\pi}{2}J_k\left(\frac{mN_{\mathrm{c}}M\pi}{2N_{\mathrm{P}}}\right)\\ \begin{cases}\dfrac{\sin(n+k)y_{l-1}-\sin(n+k)y_l}{n+k}+\dfrac{\sin(n-k)y_{l-1}-\sin(n-k)y_l}{n-k}, & k\neq n\\ [y_{l-1}-y_l+\dfrac{1}{2k}(\sin 2ky_{l-1}-\sin 2ky_l)], & k=\pm n\end{cases}\end{array}\right]$$
$$(m=2kN_{\mathrm{P}},k=1,2,3\ldots\quad n=\pm1,\pm3,\pm5,\ldots) \quad (31)$$

TABLE 2. Switching angle of the module in the i-th CPS-PWM mode.

Parameter	Value
U_L,U_N	380V，311V
S_N	10kVA
f_N	50Hz
L_f, r_f, C_f, R_d	L_f=2mH, r_f=0.01Ω C_f=25μF, R_d=0.5Ω
L_g, r_g	L_g=0.2mH, r_g=0.7Ω
N_c	8
f_s	5kHz
f_c	2kHz
V_{dc}*	48V
C_{dc}	3mF
C_B	12Ah

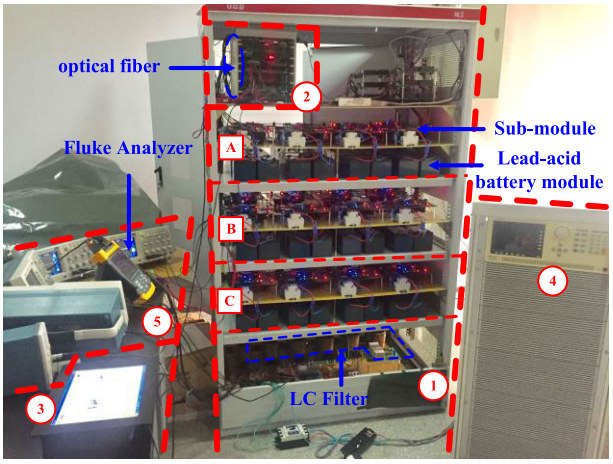

FIGURE 8. Photograph of prototype.

load, and the load power at the rated voltage $P_L = 5.4$ kW, $Q_L = -4.8$ kVar.

When the system operates in island mode, the frequency and voltage amplitude of the MMC system are fixed, in which the AC-side output voltage peak value is $U_{om} = 311$V, and the modulation ratio is set to $M \approx 0.81$. Accordingly, the amplitude of each harmonic can be calculated using Eq.(33). To validate the proposed strategy, this paper presents the comparison results of the output voltage u_x, which under the three cases of $N_p = 1$, 4, and 8.

In the third section, we analyzed the principle of NHPWM and found that for our experimental prototype with $N_c = 8$ modules, setting the experimental condition to $N_p = 1$ results in traditional HPWM modulation, while setting $N_p = 8$ results in traditional CPS-PWM modulation. Thus, we can compare the advantages of NHPWM to traditional HPWM and CPS-PWM modulation using the experimental results of $N_p = 1$, 4, and 8.

Figure 9 shows the voltage output waveform of the traditional HPWM modulation ($N_p = 1$), and Figure 10 compares the experimental output voltage harmonic spectrum to its corresponding theoretical calculation results. Figures 11-12 display the experimental results of the proposed NHPWM, and Figures 13-14 show the experimental results of CPS-

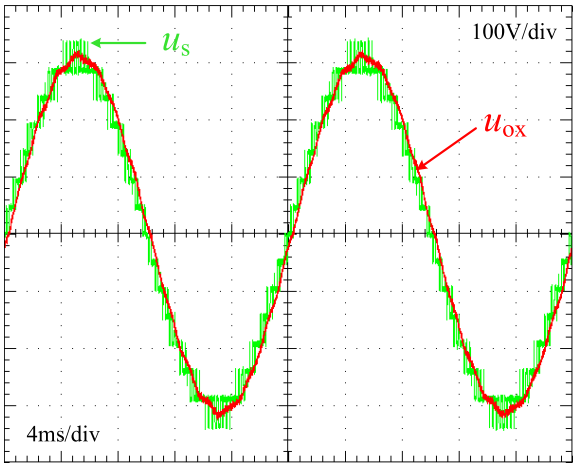

FIGURE 9. Waveforms of u_x and u_{ox} when $N_P = 1$ (HPWM).

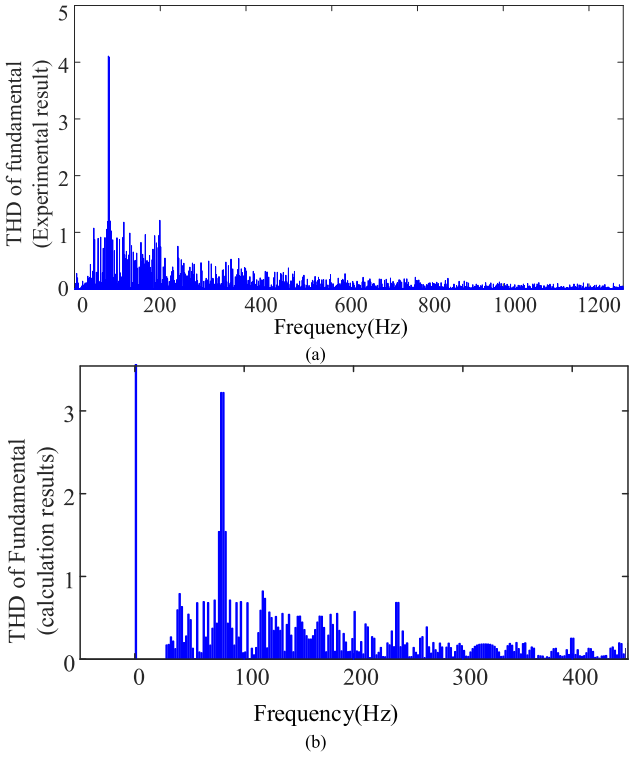

FIGURE 10. (a) FFT analysis of the experimental u_x when $N_P = 1$. (b) Harmonic calculation result when $N_P = 1$.

PWM. By analysing and comparing these results, we can evaluate the advantages of NHPWM over traditional HPWM and CPS-PWM modulation.

From the above experimental results, it can be concluded that with an increase in N_P, which is the number of modules working under the CPS-PWM modulation mode, the PWM waves on each level become denser. The experimental results of the u_x harmonic distribution in the three cases were consistent with the theoretical calculation. In the three cases of $N_p = 1$, 4, and 8, the harmonics of the output voltage are

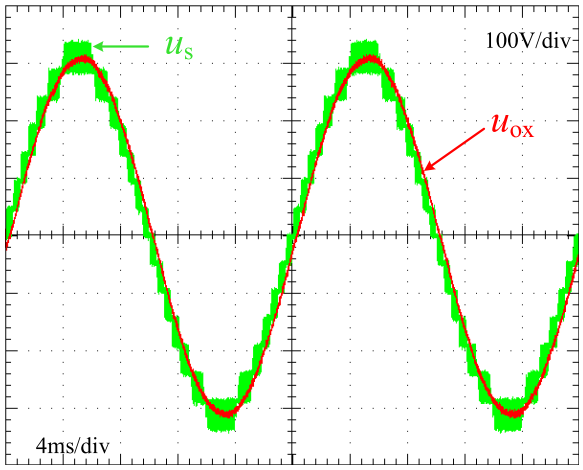

FIGURE 11. Waveforms of u_x and u_{ox} when $N_P = 4$ (NHPWM).

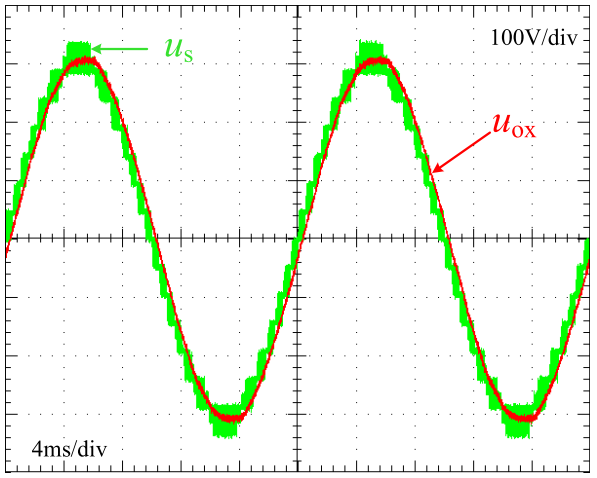

FIGURE 13. Waveforms of u_x and u_{ox} when $N_P = 8$ (CPS-PWM).

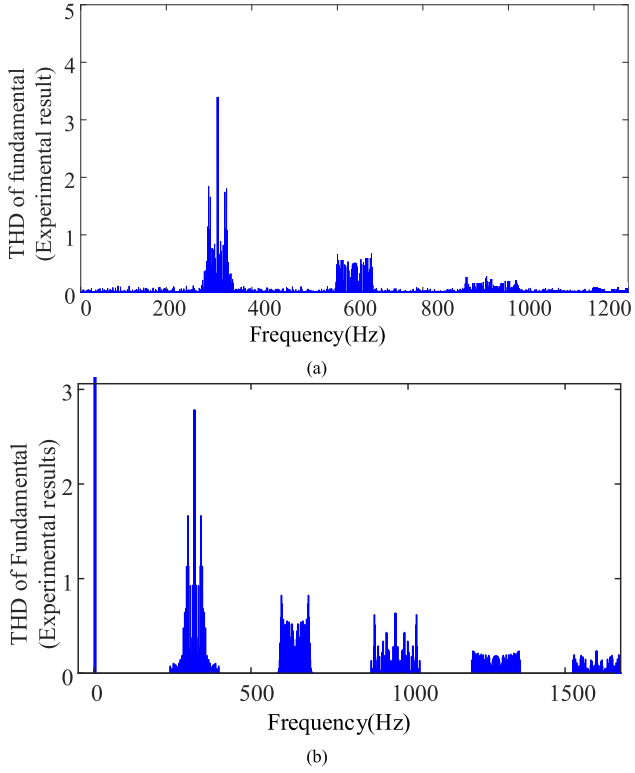

FIGURE 12. (a) FFT analysis of the experimental u_x when $N_P = 4$. (b) Harmonic calculation result when $N_P = 4$.

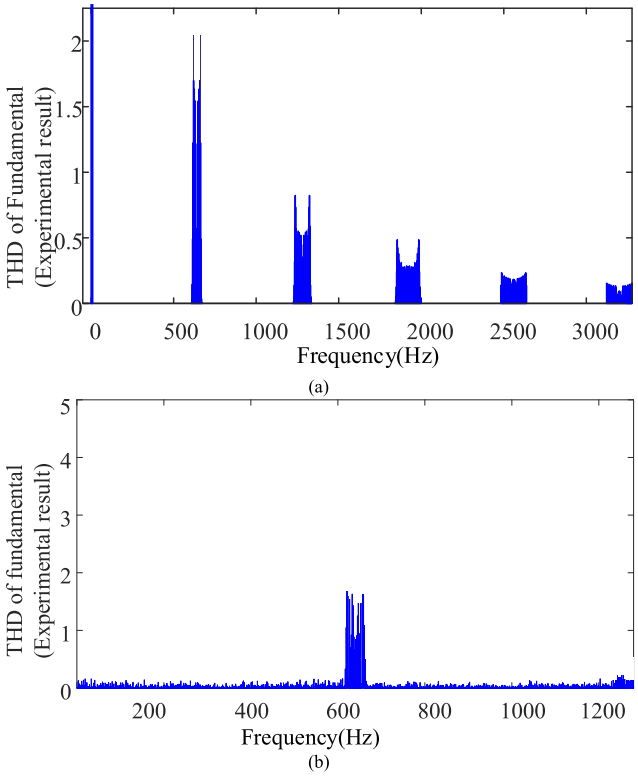

FIGURE 14. (a) FFT analysis of experimental u_x when $N_P = 8$; (b) Harmonic calculation result when $N_P = 8$.

distributed on the frequency bands of 80k, 320k and 640k respectively, and the harmonics are mainly distributed on the side frequency band of the frequency $2kN_Pf_c$ (carrier ratio $f_c/f_N = 40$). The experimental results provide a mathematical approach for the harmonic distribution of the proposed NHPWM.

According to the modulation principle of NHPWM, the total harmonic distortion THD rate of the output voltage u_x of the N_P changing converter has no effect. However, this can affect the harmonic band distribution. Because the output passive-damping LC filter parameters are fixed, they have no effect on each frequency band. The harmonic attenuation abilities are different. With an increase in N_P, the harmonic band of u_x on the spectrum gradually shifts to the right, causing the THD of the output voltage of the energy storage system u_{ox} to gradually decrease. However, when N_P increases to a certain extent, the frequency of the first harmonic band is $2N_Pf_c$ It is already high enough. The attenuation of the harmonics by the

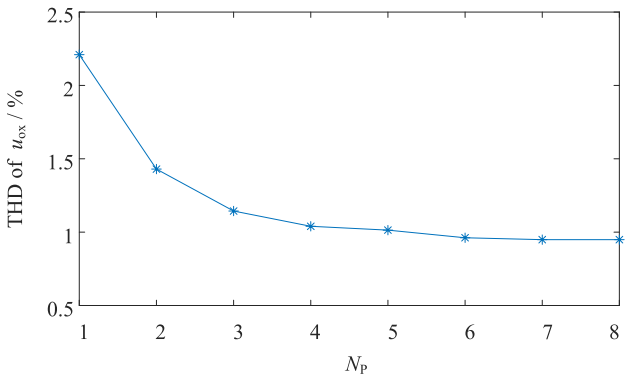

FIGURE 15. THD experimental results for the output voltage u_{ox} of the MMC energy storage system at different N_P.

LC filter is sufficiently large, and if N_P is increased, the THD of u_{ox} will change slightly.

Figure.15 shows the THD change trend of the output voltage of the energy storage system when N_P increased from 1 to 8 in the experiment. It can be seen that when $N_P \geq 4$, the THD of u_{ox} is unchanged, and increasing N_P does not make much sense.

Comparing the experimental results, it can be seen that the NHPWM proposed in this paper has lower THD performance than the traditional HPWM modulation, and almost the same THD as pure CPS-PWM. Moreover, due to the fewer switching times, the NHPWM has lower switching loss and thus higher efficiency than CPS-PWM.

V. CONCLUSION

This study introduces a modular multilevel converter battery energy storage system and establishes a mathematical model of the AC/DC modes of the system. A novel hybrid modulation strategy is proposed that combines nearest level modulation and carrier phase-shifted PWM. The NHPWM strategy can be flexibly configured for each sub-module to achieve lower output harmonic components with lower switching losses. A calculation method is proposed based on the theory of double Fourier series expansion to derive the analytical solution of the NHPWM harmonic distribution, which gives an accurate harmonic distribution of the output voltage under the NHPWM strategy. Finally, an experimental prototype was built in the laboratory, and relevant experimental tests were conducted. From the experimental results, it can be seen that the proposed NHPWM has better harmonic characteristics compared to the traditional HPWM, and has better system efficiency compared to CPS-PWM. The experimental results confirm that the NHPWM proposed in this study has better performance than traditional modulation methods, which is consistent with the theoretical analysis.

ACKNOWLEDGMENT

The author Dongdong-Chen is incredibly grateful for the arrival of his daughter Zhixi-Chen and for the joy and love, she has already brought into his life. He wishes her a healthy and happy growth.

REFERENCES

[1] P. M. Meshram and V. B. Borghate, "A simplified nearest level control (NLC) voltage balancing method for modular multilevel converter (MMC)," *IEEE Trans. Power Electron.*, vol. 30, no. 1, pp. 450–462, Jan. 2015.

[2] W. Strunk and E. B. White, *The Elements of Style*. 3rd ed. New York, NY, USA: Macmillan, 1979.

[3] L. Lin, Y. Lin, Z. He, Y. Chen, J. Hu, and W. Li, "Improved nearest-level modulation for a modular multilevel converter with a lower submodule number," *IEEE Trans. Power Electron.*, vol. 31, no. 8, pp. 5369–5377, Aug. 2016.

[4] W. Wang, K. Ma, and X. Cai, "Flexible nearest level modulation for modular multilevel converter," *IEEE Trans. Power Electron.*, vol. 36, no. 12, pp. 13686–13696, Dec. 2021.

[5] Z. Sarwer, M. D. Siddique, A. Sarwar, M. Zaid, A. Iqbal, and S. Mekhilef, "A switched-capacitor multilevel inverter topology employing a novel variable structure nearest-level modulation," *Int. Trans. Elect. Energy Syst.*, vol. 31, no. 12, 2021, Art. no. e13151.

[6] J. Cheng, T. Xu, D. Chen, and G. Chen, "Dynamic and steady state response analysis of selective harmonic elimination in high power inverters," *IEEE Access*, vol. 9, pp. 75588–75598, 2021.

[7] H. Behbahanifard, S. Abazari, and A. Sadoughi, "New scheme of SHE-PWM technique for cascaded multilevel inverters with regulation of DC voltage sources," *ISA Trans.*, vol. 97, pp. 44–52, Feb. 2020.

[8] B. Jacob and M. R. Baiju, "A new space vector modulation scheme for multilevel inverters which directly vector quantize the reference space vector," *IEEE Trans. Ind. Electron.*, vol. 62, no. 1, pp. 88–95, Jan. 2015.

[9] Y. Huang, Y. Xu, W. Zhang, and J. Zou, "Hybrid RPWM technique based on modified SVPWM to reduce the PWM acoustic noise," *IEEE Trans. Power Electron.*, vol. 34, no. 6, pp. 5667–5674, Jun. 2019.

[10] Z. Liu, Z. Zheng, S. D. Sudhoff, C. Gu, and Y. Li, "Reduction of common-mode voltage in multiphase two-level inverters using SPWM with phase-shifted carriers," *IEEE Trans. Power Electron.*, vol. 31, no. 9, pp. 6631–6645, Sep. 2016.

[11] M. Ye, L. Chen, L. Kang, S. Li, J. Zhang, and H. Wu, "Hybrid multicarrier PWM technique based on carrier reconstruction for cascaded H-bridge inverter," *IEEE Access*, vol. 7, pp. 53152–53162, 2019.

[12] Y. Li, Y. Wang, and B. Q. Li, "Generalized theory of phase-shifted carrier PWM for cascaded H-Bridge converters and modular multilevel converters," *IEEE J. Emerg. Sel. Topics Power Electron.*, vol. 4, no. 2, pp. 589–605, Jun. 2016.

[13] Y. Wang, C. Hu, R. Ding, L. Xu, C. Fu, and E. Yang, "A nearest level PWM method for the MMC in DC distribution grids," *IEEE Trans. Power Electron.*, vol. 33, no. 11, pp. 9209–9218, Nov. 2018.

[14] A. Moeini, H. Zhao, and S. Wang, "Improve control to output dynamic response and extend modulation index range with hybrid selective harmonic current mitigation-PWM and phase-shift PWM for four-quadrant cascaded H-bridge converters," *IEEE Trans. Ind. Electron.*, vol. 64, no. 9, pp. 6854–6863, Sep. 2017.

[15] M. Tariq, M. Meraj, A. Azeem, A. I. Maswood, A. Iqbal, and B. Chokkalingam, "Evaluation of level-shifted and phase-shifted PWM schemes for seven level single-phase packed U cell inverter," *CPSS Trans. Power Electron. Appl.*, vol. 3, no. 3, pp. 232–242, Sep. 2018.

[16] S. Xu, Z. Sun, C. Yao, K. Liu, and G. Ma, "Open-switch fault-tolerant operation of T-type active neutral-point-clamped converter using level-shifted PWM," *IEEE Trans. Circuits Syst. II, Exp. Briefs*, vol. 68, no. 7, pp. 2598–2602, Jul. 2021.

[17] E.-J. Lee, S.-M. Kim, and K.-B. Lee, "Modified phase-shifted PWM scheme for reliability improvement in cascaded H-Bridge multilevel inverters," *IEEE Access*, vol. 8, pp. 78130–78139, 2020.

[18] Y. Zhang, K. Dai, C. Xu, Y. Kang, and Z. Dai, "Multiple sampling PSC-PWM with hierarchical control architecture for MMC-DSTATCOM," *IET Electr. Power Appl.*, vol. 13, no. 10, pp. 1431–1440, Oct. 2019.

[19] T. Kaliannan, J. R. Albert, D. M. Begam, and P. Madhumathi, "Power quality improvement in modular multilevel inverter using for different multicarrier PWM," *Eur. J. Elect. Eng. Comput. Sci.*, vol. 5, no. 2, pp. 19–27, 2021.

[20] J. Huang and K. Li, "Suppression of common-mode voltage spectral peaks by using rotation reverse carriers in sinusoidal pulse width modulation three-phase inverters with CFM," *IET Power Electron.*, vol. 13, no. 6, pp. 1246–1256, May 2020.
[21] S. Suman, R. Mohanty, and D. Chatterjee, "Comparison of multi-carrier MLI, CHB-MLI, SHEPWM and SPWM inverters for PV-grid integration," in *Advances in Thermofluids and Renewable Energy*. Singapore: Springer, 2022, pp. 669–681.
[22] S. Xu, J. Zhang, G. Ma, Z. Sun, K. Liu, and C. Yao, "Operation of a seven-level T-type active neutral-point-clamped converter with modified level-shifted PWM," *IEEE Trans. Ind. Electron.*, vol. 68, no. 11, pp. 10970–10981, Nov. 2021.
[23] D. Chen, L. Xiao, W. Yan, and Y. Guo, "A novel hybrid modulation strategy for MMC energy storage system," in *Proc. Int. Conf. Power Energy Syst. Appl. (ICoPESA)*, Feb. 2022, pp. 144–148, doi: 10.1109/ICoPESA54515.2022.9754404.

DONGDONG CHEN received the B.S. degree in electronic information engineering from Zhejiang University, Hangzhou, China, in 2013, and the Ph.D. degree in electrical engineering from the College of Electrical Engineering, Zhejiang University, in 2018.

He is currently a Vice Professor with the Minnan University of Science and Technology. His research interests include power electronic system design, power converter digital control, and optimal design.

LONG XIAO received the B.S. degree in software engineering from the Wuhan University of Science and Technology, Wuhan, China, in 2012, the B.S. degree in optoelectronic information engineering from the Huazhong University of Science and Technology, Wuhan, in 2012, the M.S. degree in software engineering from the Wuhan University of Science and Technology, in 2014, and the Ph.D. degree in electrical engineering from the College of Electrical Engineering, Zhejiang University, Hangzhou, China, in 2019. He is currently a Vice Professor with the Minnan University of Science and Technology. His research interests include power semiconductor device modeling and driving, power converter digital control, and optimal design.

WANQING SONG received the B.Sc. degree from the Inner Mongolia University of Science and Technology, Inner Mongolia, China, in 1983, the M.Sc. degree from the University of Science and Technology Beijing, Beijing, China, in 1990, and the Ph.D. degree from Donghua University, Shanghai, China, in 2010. He is currently a Professor with the Shanghai University of Engineering Science, Shanghai. His research interests include condition monitor and fault diagnosis, big data analysis, health, and reliability.